minerals

MDPI

Article

Density Functional Theory Study of the Crystal Structure and Infrared Spectrum of a Synthetized Ettringite Mineral

Francisco Colmenero, Ana María Fernández *, Oscar Almendros-Ginestà and Tiziana Missana

Centro de Investigaciones Energéticas Medioambientales y Tecnológicas, 28040 Madrid, Spain; francisco.colmenero@ciemat.es (F.C.); oscar.almendros@ciemat.es (O.A.-G.); tiziana.missana@ciemat.es (T.M.)
* Correspondence: anamaria.fernandez@ciemat.es

Abstract: One of the most important hydration phases of Portland cement is ettringite, a calcium sulfo-aluminate mineral ($Ca_6Al_2(OH)_{12}(SO_4)_3{\cdot}26H_2O$) showing a great capacity of adsorbing radionuclides and other contaminant cationic and anionic species, or incorporating them into its crystal structure. In this work, the X-ray diffraction pattern and infrared spectra of a synthetized ettringite sample are recorded and simulated, employing theoretical methods based on Density Functional Theory. Despite the complexity of this phase, the calculated structure, X-ray diffraction pattern and infrared spectrum are in excellent agreement with their experimental counterparts. Since the calculated and experimental spectra are consistent, the main infrared bands are assigned using a normal coordinate analysis, some of them being completely reassigned with respect to other experimental works. The good agreement found provides strong support for the computational methods employed towards their use for studying the surface adsorption properties and the incorporation of contaminations in its structure. The density of reactive groups at the surfaces of ettringite is reported, and the surface adsorption of water molecules is studied. These surfaces appear to be highly hydrophilic, in agreement with the experimental finding that the ettringite structure may include more water molecules, at least up to 27, one more than in its standard formula.

Keywords: cementitious materials; density functional theory methods; Ettringite; crystal structure; X-ray diffraction; infrared spectra; thermogravimetry; surface adsorption

Citation: Colmenero, F.; Fernández, A.M.; Almendros-Ginestà, O.; Missana, T. Density Functional Theory Study of the Crystal Structure and Infrared Spectrum of a Synthetized Ettringite Mineral. *Minerals* **2024**, *14*, 824. https://doi.org/10.3390/min14080824

Academic Editor: Gianfranco Ulian

Received: 27 June 2024
Revised: 8 August 2024
Accepted: 10 August 2024
Published: 14 August 2024

1. Introduction

Cement paste is intended to be used for the immobilization of processed low and medium radioactive waste and for the construction of engineered barrier systems in deep nuclear repositories [1–3]. Therefore, the understanding of the interactions of radionuclides with solid cement phases is crucial for ensuring the long-term confinement of radioactive nuclear waste and optimizing the performance and properties of barrier solid materials [4–11]. Since cements are complex materials containing a large number of different phases [12] and evolve chemically with time, the understanding of the radionuclide retention mechanisms is still an issue. The contact of cement with water is a hazard due to the dissolution/precipitation processes leading to the transport of chemical species by diffusion and chemical reactions, leading to material degradation [3,13–15]. Understanding hydration and adsorption mechanisms in cement [16,17] is crucial in materials science since if the barrier systems are degraded, water may be the vehicle leading to the transport of radionuclides from the repositories to the biosphere. However, since cements are complex multi-component assemblages, their description requires knowledge of the properties of the individual phases. Another important issue, which may be tackled, is the simultaneous interaction of cement materials with organic molecules since their presence may facilitate or inhibit the adsorption of contaminants [18–20].

Several techniques have been employed in order to study the charge surface and adsorption properties in cementitious materials, such as electrophoretic measurements (ζ-potential), geochemical modeling, EXAFS and other types of spectroscopy techniques [4,5,21–30]. These studies have

allowed for the development of different empirical sorption models [5,16,31–33]. In a latter work [34], the surface potential (ζ-potential) of solid ettringite was measured by laser Doppler electrophoresis, in different alkaline waters with varying pH, calcium and sulfate contents. These measurements together with the theoretical results obtained in this work have been the basis for developing a simple geochemical model capable of reproducing the charging behavior of ettringite [34]. However, while the use of these empirical models is very useful in interpreting the sorption of radionuclides and predicting their behavior under variable chemical conditions, the application of mechanistic sorption models is still limited. An alternative to these models is the use of theoretical methods to investigate radionuclide adsorption mechanisms. These theoretical methods have long been used to study the surface adsorption or incorporation mechanisms and adsorbate molecules or ions in different absorbents [35–43]. However, their application for cements has been quite limited and restricted to the use of force field methods [44–52]; the use of higher-accuracy theoretical methods has only been employed scarcely [48,53–55]. Among the individual components of Portland cements [56], ettringite ($Ca_6Al_2(OH)_{12}(SO_4)_3{\cdot}26H_2O$) [57–60] is an important component because its structure includes abundant structural water and hydroxyl groups, and therefore, ettringite has the capacity to incorporate anionic species in the structure via substitution for sulfate (SO_4^{2-}), such as pertechnetate (TcO_4^-), chromate (CrO_4^{2-}), iodate (IO_3^-), selenate (SeO_4^{2-}), arsenate (AsO_4^{2-}) and others [55,61–66]. In addition, ettringite may adsorb cationic elements via substitution for Ca^{2+}, such as Sr^{2+}, Zr^{4+}, Cr^{3+}, Cd^{2+} and Co^{2+} [64,67–69]. The ettringite mineral phase is normally found in Portland cements, and its formation conditions are well known [70,71]. Calcium sulfate compounds, such as gypsum, added deliberately to Portland cement to control hydration reactions, improve its strength and reduce drying shrinkage, or when present in supplementary cementitious materials, react with calcium aluminate in the cement to form ettringite. Ettringite is a minor mineral phase in cement whose presence and amount depends on the composition of cement and its degradation state. The physical properties of this phase as the mechanical and thermodynamical ones have been extensively investigated both experimentally and theoretically [7,28,72–79]. The purpose of this work is the theoretical description of ettringite towards its use for modeling its surface properties and reactivity. The first step in this study is the computation of the structure of ettringite and the associated X-ray diffraction pattern and infrared spectrum to assess the accuracy of the model. From the computed structure, the analysis of the mineral surfaces allows for correlating the structural properties of their surface hydroxyls and adsorption sites with the ettringite reactivity.

The ultimate objective of this study is to determine the type and relative density of surface functional groups as fundamental information for the application of sorption models. Additionally, the adsorption of water molecules in the material has also been calculated, showing the highly hydrophilic character of the material.

2. Materials and Methods

2.1. Experimental

Due to the importance of ettringite, the synthetic methods of this phase are well-known [80]. In this work, the experiments were performed with a crystalline powder sample of ettringite synthesized in CIEMAT laboratories using a modification of the methods described by Odler and Abdul-Maula [81] and Warren and Reardon [82]. The synthesis was performed by mixing aluminum sulfate $Al_2(SO_4)_3{\cdot}18H_2O$ and calcium hydroxide $Ca(OH)_2$ and NaOH solutions inside an anoxic glove box and heating the suspension under stirring to 60 °C for 48 h. The precipitate was filtered, dried and stored at room temperature in the glove box.

The powder X-ray diffraction (XRD) pattern of the synthetized ettringite was recorded using a Philips X'Pert–PRO diffractometer and an anticathode Cu-K_α at 45 kV and 40 mA, equipped with a fixed divergence slit (0.1245° size), Scientific X'celerator detector and R-T Spinner PW3064. The samples were investigated from 2° to 80° 2θ with a step size of

0.017° 2θ and a scan rate of 50 s per step. The identity of the material was confirmed by XRD analysis using the Power Diffraction File database from the International Center for Diffraction Data (ICDD) [83].

The Fourier-transform infrared (FTIR) spectrum of ettringite was measured in the middle-IR region (4000–400 cm^{-1}) using a Nicolet iS50 spectrometer with a DTGS KBr detector (resolution 4 cm^{-1}, 32 scans) on KBr-pressed discs in the transmission technique in an atmosphere continuously purged from water and atmospheric CO_2. Two milligrams of the powdered air-dried sample were dispersed in 200 mg of KBr and pressed to a clear disc. The pressed samples were analyzed at room temperature and then heated in an oven overnight at 110 °C. All spectral manipulations were carried out using Omnic 9 software [84].

The thermal behavior of the synthetized mineral was studied using Setaram Themys TG-DSC equipment at a heating rate of 10 K/min, under dynamic argon flow (20 mL/min), at temperatures between 20 and 1100 °C. The termogravimetric analyzer and the DSC calorimeter were calibrated on temperature and enthalpy values based on the melting points of standard reference metals (In, Sn, Pb, Zn, Al, Ag, Au, Ni). The temperature was measured accurately to ±0.1 °C. The calorimetric precision was ±1%. The mass of ettringite was ~35 mg.

2.2. Theoretical

The crystal structure and infrared spectrum of ettringite were modeled by employing the CASTEP program [85], a component of the Materials Studio program suite [86]. The theoretical treatment employed is based on Periodic Density Functional Theory using plane wave basis sets and pseudopotentials [87]. The computations were carried out using the Perdew–Burke–Ernzerhof [88] density functional complemented with Grimme's dispersion correction (DFT-D2) [89]. The specific pseudopotentials utilized were norm-conserving pseudopotentials [90] included in CASTEP code.

The ettringite unit cell, $Ca_6Al_2(OH)_{12}(SO_4)_3{\cdot}26H_2O$[58], is trigonal with sides of $a = b$ = 11.2 Å and c = 21.4 Å and contains 256 atoms. Since the unit cell of ettringite is quite large, supercells have not been employed in the calculations. Some trial calculations performed using a 2 × 2 × 1 supercell have produced nearly the same results as those performed using a single unit cell. The unit cell parameters and atomic positions were optimized by means of the BFGS technique. A plane wave kinetic energy cut-off parameter of ε = 900 eV and a Monkhost-Pack κ-mesh of 2 × 2 × 2 [91] were employed. The initial reference structure for the calculations was that of Hartman and Berliner [58], obtained by the refinement of X-ray diffraction data from a synthetic ettringite sample.

The geometry optimizations of the ettringite structure with and without adsorbed water molecules were performed by employing the Broyden–Fletcher–Goldfarb–Shanno scheme (BFGS) [92]. The software REFLEX included in the MaterialsStudio software package was used to derive the X-ray powder diffraction patterns [93] from the computed and experimental crystal structures [94]. The computation of the infrared spectrum of ettringite was performed by means of density functional perturbation theory, as implemented in the CASTEP program [95,96]. The initial determination of the most stable adsorption sites for water molecules inside the ettringite structure were performed using Monte Carlo simulations employing the Adsorption Locator module [97] implemented in the Materials Studio program suite. Monte Carlo simulations were employed to randomly sample the energy of different water–surface configurations in order to find the most stable ones. In these initial simulations, the COMPASSIII [98] force field was employed. This force field was chosen because it is optimized for condensed-phase applications [99]. The results of these force field-based simulations were then improved using full geometry DFT optimizations of ettringite with adsorbed water molecules at different initial adsorption sites. For this purpose, the (1 0 0), (0 1 0) and (0 0 1) surfaces were created using Materials Studio by cleaving or cutting a surface along these specific planes and a vacuum slab space on top of these surfaces with a length of approximately 10 Å. Then, the water molecules were placed near the ad-

sorption sites and the geometry was fully optimized using stringent convergence thresholds in the variation of the total energy, maximum atomic force, maximum atomic displacement and maximum stress of 2.5×10^{-6} eV/atom, 0.005 eV/Å, 2.5×10^{-4} Å and 0.0025 GPa, respectively. All the located adsorption sites were probed. Only the adsorption of single water molecules was investigated.

3. Results and Discussion

3.1. Crystal Structure

The computed crystal structure of ettringite from the [0 0 1] direction is shown in Figure 1. The crystal structure of ettringite [57–60] contains columns with the formula $[Ca_3Al(OH)_6 \cdot 12H_2O]^{3+}$ expanding along the direction of the *c* axis, which are composed of $Al(OH)_6$ octahedra alternating with triangular groups of edge-sharing CaO_8 polyhedra. Four of the oxygen atoms coordinating the Ca atom are from H_2O molecules, which form the cylindrical surface of the column (see Figure 1). The columns delimitate channels containing sulfate ions and zeolitic water. The different columns are linked through the sulfate ions via hydrogen bonds. The structural formula is $[Ca_6Al_2(OH)_{12} \cdot 24H_2O]^{6+}[(SO_4)_3 \cdot 2H_2O]^{6-}$, where the first and second bracket correspond to the columns and the channels, respectively.

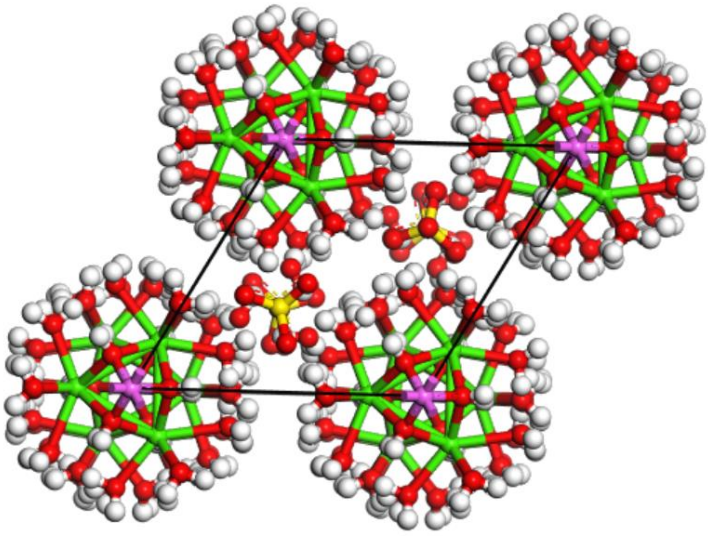

Figure 1. Computed crystal structure of ettringite from the [100] direction. Color code: Ca—violet; A—green; O—red; S—yellow: H—white.

Ettringite has trigonal symmetry and crystallizes in the *P*31*c* space group. The computed unit cell parameters are given in Table 1, together with the experimental ones obtained in previous investigations. While the parameters reported by Moore and Taylor [57], Hartman and Berliner [58] and Goetz-Neunhoeffer and Neubauer [59] are deduced from synthetic samples, those given by Gatta et al. [60] and Scholtzová et al. [76] were determined from natural mineral samples. As can be observed, the differences between the different parameter sets are relatively small. The values obtained for the lattice parameters, $a = b = 11.21$ Å and $c = 21.14$ Å, are in excellent agreement with the experimental ones $a = b = 11.17$ Å and $c = 21.35$ Å [58]. The computed unit cell volume differs from the experimental one by only 0.3%. The structure of ettringite was also computed by Scholtzová et al. [76], and the corresponding lattice parameters are shown in Table 1 for comparison. These authors also experimentally studied a natural mineral from Wessels Mine, Northern Cape Province, South Africa by single-crystal X-ray diffraction spectroscopy and FTIR spectroscopy. As can be seen, the computed DFT parameters provided by these authors are in worse agreement with the experiment than the DFT-D2 parameters obtained in this work. DFT-D2 parameters represent an improvement in the accuracy of prediction. For example, the unit cell volume is overestimated by 3.4% with respect to the experimental

value of Hartman and Berliner [58]. In the work by Scholtzová et al., the VASP code together with the projector-augmented-wave (PAW) method were employed with an energy cut-off of 500 eV and a κ mesh of 1 × 1 × 1. In the present work, we used the CASTEP program with norm-conserving pseudopotentials with an energy cut-off of 900 eV and a κ-mesh of 2 × 2 × 2. Thus, while the comparison is quite difficult due to the different kinds of methods employed and both calculations should be accurate enough, our DFT-D2 calculation parameters should be of a higher quality, since they include Grimme's dispersion correction, which, generally, significantly improve the computed crystal structures of materials containing a high number of water molecules.

Table 1. Computed unit cell parameters of ettringite. In the table, ΔV(%), represents the percentage difference of the unit cell volume with respect to the reference parameters from Hartman and Berliner [58].

Parameter	*a* (Å)	*b* (Å)	*c* (Å)	*α*(deg)	*β*(deg)	*γ*(deg)	Vol. (Å^3)	Δ*V*(%)	*ρ* (g/cm^3)
Exp. [1]	11.203 (2)	11.203 (2)	21.467 (4)	90.0	90.0	120.0	2333.0 (8)	1.17	1.784
Exp. [2]	11.166881 (82)	11.166881 (82)	21.35366 (22)	90.0	90.0	120.0	2306.039 (3)	0.0	1.791
Exp. [3]	11.1710	11.1710	21.3640	90.0	90.0	120.0	2308.858	0.12	1.831
Exp. [4]	11.26	11.26	21.48	90.0	90.0	120.0	2358.53	2.28	1.759
Exp. [5]	11.229 (1)	11.229 (1)	21.478 (3)	90.0	90.0	120.0	2345.34 (6)	1.70	1.777
DFT-D2	11.2152	11.2152	21.1403	90.0	90.0	120.0	2298.419	−0.33	1.811
DFT [1]	11.223	11.223	21.867	90.0	90.0	120.0	2385.401	3.44	1.146

[1] Scholtzová et al. [76]; [2] Hartman and Berliner [58]; [3] Gatta et al. [60]; [4] Moore and Taylor [57]; [5] Goetz-Neunhoeffer and Neubauer [59].

3.2. X-ray Diffraction Pattern

From the structure of ettringite calculated theoretically, the X-ray powder pattern was derived. The resulting pattern is compared with the experimental one in Figure 2. The positions of the main reflections are given in Table 2. As can be seen, both patterns are highly consistent. The five main reflections are calculated at °2θ = 9.15, 15.85, 22.98, 18.95 and 35.02°, which may be compared with the experimental positions at °2θ = 9.12, 15.83, 23.16, 19.14 and 35.36°.

Table 2. Most intense reflections in the X-ray diffraction pattern of ettringite derived from the (a) experimental and (b) calculated crystal structure in this work.

(*hkl*)	2θ(deg)		Δ(2θ)
	(a) Exp.	(b) Calc.	
(0 1 0)	9.149	9.121	−0.028
(−1 2 0)	15.848	15.833	−0.015
(−1 2 4)	22.976	23.159	0.183
(0 1 4)	18.950	19.142	0.192
(1 2 6)	35.021	35.361	0.340
(0 3 4)	32.315	32.484	0.169
(2 2 6)	40.895	41.210	0.315
(−1 2 6)	29.180	29.991	0.811
(1 2 2)	25.682	25.734	0.052
(−1 2 2)	17.894	17.936	0.042
(1 3 6)	41.984	42.298	0.314
(−1 4 2)	34.328	34.417	0.089
(0 3 0)	27.563	27.602	0.039
(0 1 1)	10.073	10.039	−0.034
(0 0 8)	33.404	33.962	0.558
(0 2 4)	24.758	24.937	0.179
(0 0 2)	8.324	8.374	0.050
(−1 4 4)	37.364	37.537	0.173
(0 1 3)	15.452	15.557	0.105

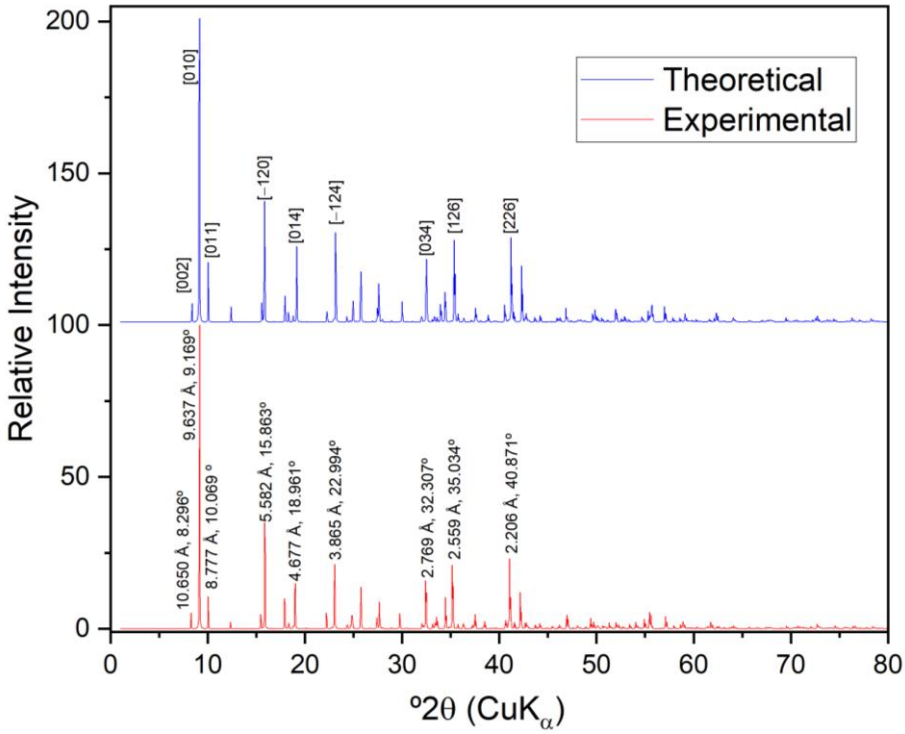

Figure 2. X-ray diffraction patterns of ettringite obtained from the computed and experimental synthetized crystal structures of ettringite.

In order to assess the differences between the X-ray diffraction pattern of the synthetized sample, the pattern derived from the crystal structure reported by Goetz-Neunhoeffer and Neubauer [59] and obtained from a synthetized sample was derived. Likewise, to evaluate the differences between the X-ray diffraction patterns of synthetized and natural samples, the pattern obtained from the crystal structure reported by Gatta et al. [60] and obtained from a natural mineral sample was also computed. The results are compared with that measured in this work in Figures S1 and S2 of the Supplementary Materials. As can be observed, all patterns are quite similar, irrespective of the nature of the sample.

3.3. Infrared Spectra

The experimental infrared spectrum of ettringite was recorded from the synthesized sample. The spectrum was also determined by using first-principles methods employing density functional perturbation theory. The infrared spectrum determined theoretically compared with the experimental infrared spectrum is shown in Figure 3, and as can be observed, both spectra are in good agreement. However, the six high-frequency bands found in the theoretical spectrum are not resolved in the experimental one, where only a broad band is observed. The large number of hydroxyl groups from Al octahedra and water molecules is the main cause of the broadening of the corresponding bands in the long wavenumber region of the measured spectrum. Since the agreement of the theoretical and the experimental spectrum was very good, a normal mode analysis was performed to assign the most intense bands in the infrared spectrum. The experimental and computed infrared band vibrational frequencies and the corresponding calculated intensities and assignments are given in Table 3. For a comparison of the results, we found in the literature an infrared spectrum measured from a natural mineral sample, which was assigned by Scholtzová, Kucková, Kozísek and Tunega [76] (SKKT). Previous infrared spectra measurements of ettringite were also performed by Frost et al. [100] and Myneni et al. [101].

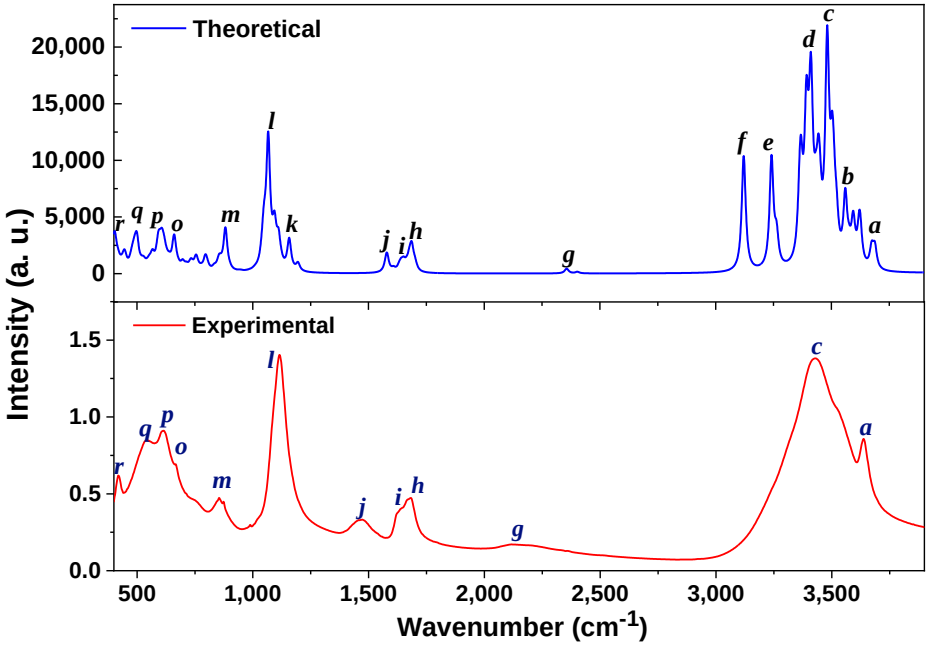

Figure 3. Computed and experimental infrared spectra of ettringite.

Table 3. Experimental and calculated infrared band wavenumbers of ettringite and calculated intensities and assignments.

Band Name	Vibrational Frequency (cm^{-1})		Assignment
	Exp.	Theor.	
a	3637	3676	ν_{OH}
	-	3622	ν_{OH}
b	-	3594	ν_{OH}
	-	3560	ν_{OH}
c	3426	3482	ν_{OH}
d	-	3411	ν_{OH}
e	-	3241	ν_{OH}
f	-	3121	ν_{OH}
g	2117	2355	$\delta(\mathrm{AlOH})$
h	1683	1685	$\delta(H_2O)$
i	1635	1651	$\delta(H_2O)$
j	1473	1579	$\delta(H_2O)$
k	1114	1157	$\nu(AlO_6) + \delta(SO_4) + T(H_2O)$
l	1011	1067	$\nu\left(SO_4^{2-}\right)$
m	988	922	$\nu\left(SO_4^{2-}\right)$
n	873	882	$l(H_2O)$
	854	863	$l(H_2O)$
o	667	660	$l(H_2O)$
p	615	606	$\tau(H_2O)$
q	542	497	$\omega(H_2O)$
r	418	403	$\omega(H_2O)$

In the higher wavenumber region [3700–3000 cm^{-1}], the theoretical spectrum has a higher resolution and displays the inner structure of the experimental spectrum. The high-wavenumber region of the experimental infrared spectrum of ettringite is very broad due to the thermal motion of the atoms in the unit cell, which produces that the different OH stretching vibrational bands overlap in a single convoluted band. DFT vibrational spectrum calculations are performed at the most stable configuration at 0 K, and, therefore, the bands do not overlap and are deconvoluted. In this region, the bands *a* and *c*

located at 3637 and 3426 cm^{-1} correspond to the theoretical bands at 3672 and 3482 cm^{-1}, respectively. These two bands are assigned to OH bond stretching vibrations (ν_{OH}). These bands were found by SKKT at 3637 and 3432 cm^{-1}, respectively. Similarly, the band *g* at 2117 cm^{-1} was not found by SKKT and is placed in the theoretical spectrum at 2355 cm^{-1}. This band is assigned to Al − OH bending vibrations ($\delta(Al-OH)$). The bands in the experimental spectrum at 1683 and 1635 cm^{-1} (*h* and *i*) are calculated to be at 1685 and 1651 cm^{-1} and assigned to H_2O bending vibrations ($\delta(H_2O)$). These bands were found at 1667 and 1633 cm^{-1} by SKKT. The band *j* at 1473 cm^{-1}, also assigned to H_2O bending vibrations, was found at 1579 cm^{-1}. This band was not found by SKKT. The bands *k*, *l* and *m* at 1114, 1011 and 988 cm^{-1} were found to be placed theoretically at 1157 and 1067 and 922 cm^{-1} (SKKT only found the bands *k* and *m* at 1113 and 989 cm^{-1} and calculated them at 1143 and 1011 cm^{-1}). The first is assigned to Al − O stretching and sulfate bending vibrations and water molecule translations ($\nu(AlO_6) + \delta(SO_4) + T(H_2O)$), and the second and third ones are assigned to sulfate stretching vibrations $\nu(SO_4^{2-})$. SKKT assigned these *k* and *m* bands differently, to asymmetric and symmetric sulfate stretching vibrations. As can be seen, for example, in Figure 4A, where the atomic motions associated with the vibrational mode $\nu = 1011$ cm^{-1} are shown, the vibrations in ettringite are neither symmetric nor antisymmetric.

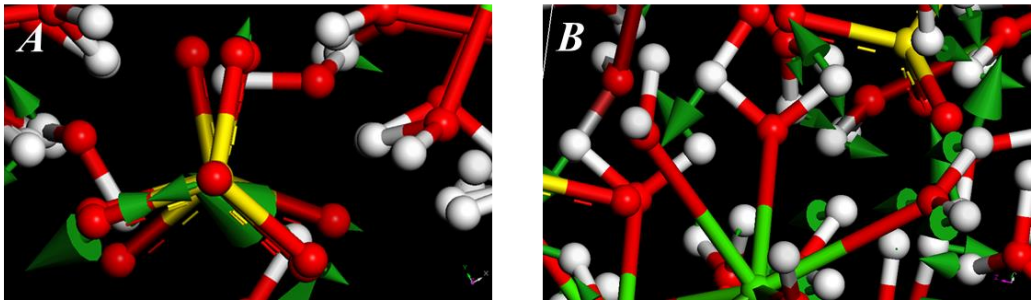

Figure 4. Computed and experimental infrared spectra of ettringite. Picture of the atomic motions associated with the infrared active vibrational normal modes of ettringite with (**A**) $\nu = 1157$ and (**B**) $\nu = 403$ cm^{-1}. The green arrows in the figures represent the direction and amplitude of atomic vibrational motions. Color code: Ca—violet; Al—green; O—red; S—yellow; H—white.

The band *n* consists of two component sub-bands at 873 and 854 cm^{-1}. These bands are found theoretically at 882 and 863 cm^{-1}, and both are assigned to water librations ($l(H_2O)$). For comparison, SKKT encountered these bands at 885 and 839 cm^{-1}. However, these authors assigned them to Al − OH bending vibrations. Finally, the bands *o*, *p*, *q* and *r* at 667, 615, 542 and 418 cm^{-1} were found theoretically at 660, 606, 497 and 403 cm^{-1} (SKKT only found the last three bands at 616, 542 and 418 cm^{-1} in the experimental spectrum but obtained all of them theoretically at 645, 582, 550 and 424 cm^{-1}). Band *o* is assigned to water librations; band *p* is assigned to water twisting ($\tau(H_2O)$) vibrations and bands *q* and *r* are assigned to water wagging vibrations. SKKT, however, assigned band *q* to S − O stretching vibrations and the remaining ones to Al − OH bending vibrations. The atomic motions associated with the vibrational mode ν = 403 cm^{-1} are displayed in Figure 4B. The vibrational frequencies and assignments performed in this work and from SKKT are compared in Table S1 of the Supplementary Materials. In Table S1, the vibrational frequencies reported by Frost et al. [100] are also given. The range of frequency covered by Frost et al. (4000–800 cm^{-1}) is smaller than that covered in the present work. It should be noted that both Scholtzová et al. [76] and Frost et al. [100] observed a band near 1410 cm^{-1} and they attributed it to a carbonate impurity in their natural ettringite samples. However, this band is not observed in our spectrum from a synthetic sample. We observed only a band at 1473 cm^{-1}, which is theoretically assigned to H_2O bending vibrations in this study. Therefore, the band observed at 1410 cm^{-1} by Scholtzová et al. [76] and Frost et al. [100]

is probably due to H_2O bending vibrations, as calculated in this work, rather than to a carbonate impurity.

3.4. Surface Adsorption

3.4.1. Density of Reactive Functional Groups

An important parameter determining the reactivity of a given material is the density of reactive functional groups at their edge surfaces, since it determines the surface charge [102]. In this work, the investigated edge surface sites of ettringite are the −CaOH and −AlOH groups at the (0 1 0), (0 1 0) and (1 0 0) surfaces. The two types of groups are equivalent in ettringite since the OH^- groups belong simultaneously to the coordination polyhedra of Ca and Al (Figure 5). As shown in Figure 6, at the (1 0 0) surface, there are 8 −CaOH/ − AlOH groups (two per Al atom in the surface). As a result, the corresponding surface density is calculated as 0.033 OH^- sites/$Å^2$ = 3.3 OH^- sites/nm^2. The (0 1 0) surface is the same as the [100] surface due to the space symmetry of ettringite. In the case of the (0 0 1) surface (Figure 7), there are 3 −CaOH/ − AlOH groups, and the corresponding surface density calculated is 0.024 OH^- sites/$Å^2$ = 2.4 sites/nm^2. While the density of reactive groups is not a new result in the sense that the crystal structure of ettringite is known, the data about surface charge density have not been previously reported. The density of surface sites available for sorption processes is essential for cationic and anionic radionuclide retention processes, and these data have been the basis for developing a geochemical surface model capable of reproducing the evolution of ettringite charge under different cement degradation stages and porewater compositions [34].

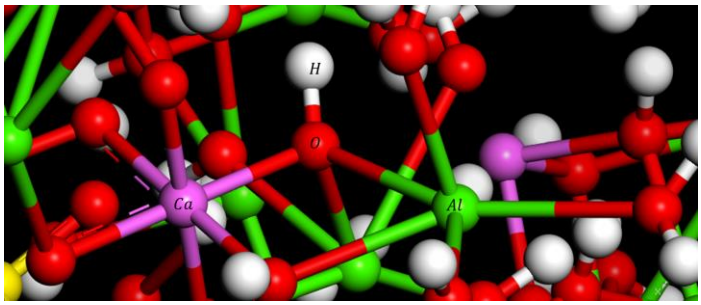

Figure 5. The −CaOH/ − AlOH groups in the (1 0 0) surface. Color code: Ca—violet; Al—green; O—red; S—yellow; H—white.

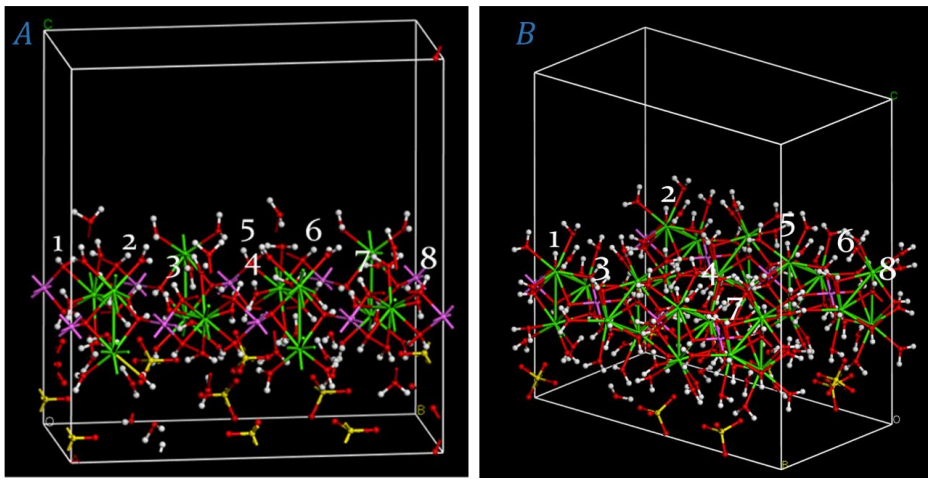

Figure 6. The −CaOH/ − AlOH groups in the (1 0 0) surface (equivalent to the (0 1 0) surface due to space symmetry) of ettringite from two different orientations (**A**,**B**). The numeric labels enumerate the different reactive groups (1 to 8). Color code: Ca—violet; Al—green; O—red; S—yellow; H—white.

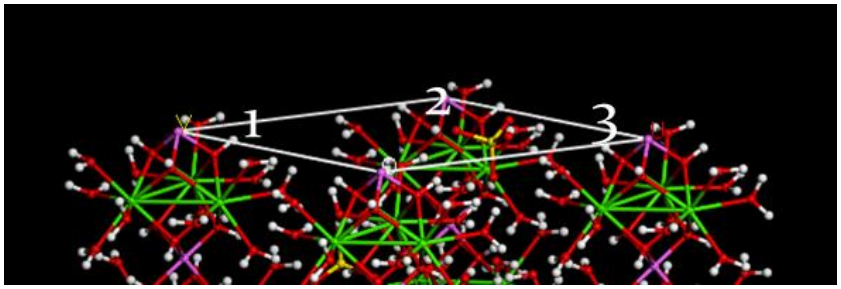

Figure 7. The OH^- groups in the (0 0 1) surface of ettringite. The numeric labels enumerate the different reactive groups (1 to 3). Color code: Ca—violet; Al—green; O—red; S—yellow; H—white.

3.4.2. Water Adsorption on the Surfaces of Ettringite

The surface adsorption of neutral molecules for ettringite has been studied over time. The adsorption of comb-shaped polycarboxylates (PCE) with different numbers of grafted sidechains on ettringite surfaces and aqueous media was analyzed by means of force-field molecular dynamics methods [48]. The backbones of PCE molecules are chemisorbed to the surfaces of ettringite, and the sidechains are extended to the aqueous phase. The adsorption of superplasticizers, such as polycarboxylic acids, naphthalene sulfonate, amino sulfonate and aliphatic compounds, was also investigated experimentally (Shi et al. [103]). Superplasticizers can change the crystal morphology and stability; polar groups of superplasticizers bond with Ca^{2+} ions to form calcium complexes. The diffusion of several species as Cs^+ and Cl^- along the nanopores of ettringite [44] and the ionic adsorption of sodium sulfate (Na_2SO_4) from an aqueous solution on the ettringite surfaces [50] have also been investigated. Great effort has been devoted to the atomistic simulation of applications of cement-related materials [104]. However, except for some recent investigations [53–55,66], these studies were mostly performed using force field methods [52]. Only the incorporation of iodate, IO_3^- [55], and arsenate, AsO_4^- [62], anionic species into the structure of ettringite has been investigated using density functional theory methods. Therefore, the adsorption at the surfaces of ettringite of different cations, anions and neutral molecules using accurate density functional methods should be studied in depth to disentangle the adsorption mechanisms.

The experimentally determined number of H_2O molecules in the unit cell, $Ca_6Al_2(OH)_{12}(SO_4)_3{\cdot}nH_2O$, varies between 24 and 27, with 26 being the most common number [57–60,105]. This water content is associated with systems at equilibrium between 10 and 96% relative humidity (RH) at ambient temperature [28,106]. Thus, ettringite's water content is variable with $(n + 6) = 30–33$, where n stands for molecular water and 6 stands for water arising from the 12 OH^- groups in the column ($6CaO{\cdot}Al_2O_3{\cdot}3CaSO_4{\cdot}(n+6)H_2O$). Most of the researchers agree on a maximum value of $(n + 6) = 32$ ($Ca_6Al_2(OH)_{12}(SO_4)_3{\cdot}26H_2O$ or $6CaO{\cdot}Al_2O_3{\cdot}3CaSO_4{\cdot}32H_2O$), 30 fixed in the columns and 2 H_2O more loosely bound in the channels as zeolitic water. The dependence of the unit cell parameters on the amount of water present is insignificant, as shown by DFT calculations [105] and in some experiments [107], but below $(n + 6) = 30$, etrringite undergoes a series of structural changes in the cell size and crystallinity (<10% RH at 25 °C) [28,57,106]. Therefore, water sorption processes play a critical role in ettringite's volume stability. The hysteresis behavior under sorption/desorption due to relative humidity and temperature variations (wetting/drying) is still under debate [28,50,106,108–110].

Analyzing the water desorption/dehydration process of this synthesized ettringite mineral (see Figures S2 and S3 in Supplementary Materials) by thermogravimetry (TG-DSC), the number of water molecules is 24.4 ($n + 6 = 30.4$), so there are 0.4 zeolitic water molecules (Table S2). This is in agreement with that found in [28,106], where it is shown that only 30 H_2O molecules take part in the formation of the crystal structure of ettringite between 5 and 85–90% RH. Thus, a problem arises concerning the arrangement of molecules

above 30 H_2O regarding whether they are located in the channels as zeolitic water, a solid solution, in lattice defects or adsorbed on the surface of the crystals [57,106].

In this work, we analyzed the adsorption of a single water molecule at the (1 0 0), (0 1 0) and (0 0 1) surfaces of this crystal structure: $Ca_6Al_2(OH)_{12}(SO_4)_3{\cdot}26H_2O$, as described in the Methods Section. After the water molecule was placed near the adsorption sites, the geometry was fully optimized. All the located adsorption sites were probed. Our DFT calculations indicate that the water molecule remained adsorbed to the (0 0 1), (0 1 0) and (0 0 1) edge surfaces by hydrogen bonding, as shown in Figure 8 for the case of the (0 0 1) surface. Thus, surface water adsorption on surfaces is accompanied by the formation of hydrogen bonds from H_2O molecules to the surface sites belonging to the Ca- and Al-polyhedra.

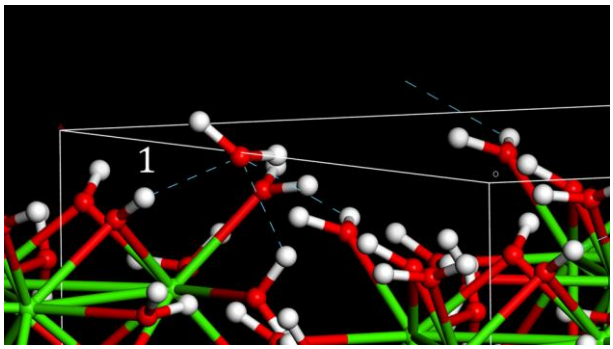

Figure 8. Adsorption of a water molecule on the (0 0 1) surface of ettringite. The numeric label is a reactive group. Color code: Al—green; O—red; H—white.

The adsorption energies of a single water molecule on the (0 0 1) and (1 0 0) (equivalent to (0 1 0)) surfaces were determined using the following equation:

$$\Delta E_{ads} = \left[E_{SLAB@H_2O} - \left(E_{SLAB} + E_{H_2O}\right)\right] \quad (1)$$

where $E_{SLAB@H_2O}$ and E_{SLAB} are the energies of the system with and without the adsorbed water molecule and E_{H_2O} is the energy of a single water molecule. The adsorption energies are in the range from −1.7 eV to −2.7 eV, which indicates that the surfaces are considerably hydrophilic and that water adsorption is energetically favorable. These adsorption energies are higher than those found by Wang et al. [111] for the adsorption of water molecules on the surfaces of β-dicalcium silicate (β–C2S) (from −0.78 to −1.48 eV).

The adsorption calculations were performed with and without ettringite surface geometry optimization (fixed surface), and similar results were obtained. In addition, the distortion of the ettringite structure due to water adsorption when a full geometry optimization was performed in the presence and absence of water molecules was found to be relatively small. For example, for the adsorption of one water molecule at one of the surface sites belonging to the (1 0 0) surface, the optimized lattice parameters were a = 21.3537 Å, b = 11.1669 Å and c = 22.5292 Å; whereas for those of bulk ettringite, without any water molecule adsorption, the optimized lattice parameters were 21.2152, 11.2152 and 21.1403 Å, respectively (the vacuum slab space was considered by increasing the lattice parameter by 10 Å).

The present results, being only focused on molecular adsorption, indicate the highly hydrophilic character of the ettringite surfaces, suggesting that the surface water adsorption may be the process for the incorporation of additional water molecules inside the structure of this mineral, which is able to incorporate from $(n + 6) = 30$ to $(n + 6) = 33$ water molecules, or even up to $(n + 6) = 36$, depending on the water vapor pressure or RH and temperature experimental conditions [106], the number of water molecules as zeolitic water at channels being 0, 3 and 6, respectively.

A standard formula of ettringite with 27 water molecules was found by Gatta et al. [60]. The optimized structure of ettringite including 27 water molecules, $(n + 6) = 33$, determined

using their reported structure as the initial structure, is given in the Supplementary Materials as a file with a CIF format. The additional water molecule included in the unit cell with 27 water molecules has a small impact on its size since the lattice parameters change only slightly (see Table 1), and the unit cell volume increases by 0.17%. This additional zeolitic water molecule located at intercolumns is highly disordered.

It is interesting to note that the structure of ettringite with 26 water molecules was derived by Hartmann and Berliner [58] by the refinement of neutron diffraction data obtained from a synthetic sample at room temperature, all the sites being modeled isotropically. However, that derived by Gata et al. [60], including 27 water molecules, was determined based on neutron diffraction data from a natural mineral sample at a low temperature (20 K), all the H sites being modeled anisotropically, and the water distribution was highly disordered. Thus, the different water content may result from the nature of the sample and the temperature at which the refinement was made.

The adsorption of multiple water molecules is possible using the same formalism as that used in this paper (Adsorption Locator Module followed by DFT calculations) and should be studied in future works.

4. Conclusions

Ettringite is an important cementitious phase because its structure includes abundant structural water and hydroxyl groups, and, therefore, ettringite has the capacity to incorporate anionic species in the structure via substitution for sulfate anion and adsorb cationic elements via substitution for calcium cation. In this work, a crystalline powder sample of ettringite synthesized in our laboratory and the X-ray diffraction pattern and Infrared spectrum were measured experimentally. The identity of the synthetized sample was confirmed by XRD analysis using the Power Diffraction File database (ICDD). Towards the study of the adsorption properties of ettringite, the crystal structure, X-ray diffraction pattern and infrared spectrum were also determined theoretically. Since the agreement in the X-ray diffraction pattern and IR spectrum was very good, the computed crystal structure and the methods used to compute were considered to be appropriate for performing a study of the adsorption properties of ettringite. Therefore, the density of reactive functional groups at their edge surfaces, an important parameter governing the material reactivity, was determined. At both the (1 0 0) and (1 0 0) surfaces, there are 8 $-$CaOH/ $-$ AlOH groups, the corresponding surface density being 3.3 OH^- sites/nm^2. At the (0 0 1) surface, there are 3 $-$CaOH/ $-$ AlOH groups, with a surface density of 2.4 sites/nm^2. Furthermore, the adsorption of water molecules at the (0 0 1), (0 1 0) and (0 0 1) surfaces was studied theoretically. In this work, it was found that water molecules remain adsorbed at these surfaces by hydrogen bonding. The adsorption energies are in the range from -1.7 eV to -2.7 eV, so the surfaces are considerably hydrophilic and water adsorption is energetically favorable This suggests that the surface water adsorption may be the initial step in the process for the incorporation of additional water molecules inside the structure of this mineral, which is able to incorporate from (n + 6) = 30 to (n + 6) = 36 (6 H_2O as zeolitic water and/or adsorbed on surfaces), depending on the water vapor pressure or RH, and temperature conditions [106].

Supplementary Materials: The following supporting information can be downloaded at: https://www.mdpi.com/article/10.3390/min14080824/s1: Figure S1: X-ray diffraction patterns of ettringite: (a) Derived from the experimental crystal structure from Goetz-Neunhoeffer and Neubauer obtained from a synthetized sample; (b) This work (synthetized sample); Figure S2: X-ray diffraction patterns of ettringite: (a) Derived from the experimental crystal structure from Gatta et al. obtained from a natural sample; (b) This work (synthetized sample); Figure S3. TG-DSC curves of the synthetized ettringite mineral (mass used = 35.511 mg); Figure S4: TG-DSC curves of the synthetized ettringite mineral (duplicate, mass used = 35.733 mg); Table S1: Experimental vibrational frequencies and assignments obtained in this work and in that from Scholtzová et al., referred to in the table as SKKT. The vibrational frequencies reported by Frost et al. are also given. Table S2. Dehydration process of synthetized ettringite based on TG-DSC analyses.

Author Contributions: Conceptualization: F.C. and T.M.; Methodology: F.C., A.M.F., O.A.-G. and T.M.; Formal analysis: F.C., A.M.F., O.A.-G. and T.M.; Investigation: F.C., A.M.F., O.A.-G. and T.M.; Writing: F.C.; Writing and editing: F.C., A.M.F., O.A.-G. and T.M. All authors have read and agreed to the published version of the manuscript.

Funding: This research was funded by the Agence national de la Reserche (ANR) and was partially supported by the European Union's Horizon 2020 Research and Innovation Programme under Grand Agreement no. 847593 (EURAD-CORI) and by the Spanish Ministry of Science Innovation (PID2019-106398GB-I00, ARNO Project). F.C. acknowledges the financial support of CNRS within the project AAPG2020–PlanetGEM: Planet differentiation: an integrated Experimental and numerical Modeling of Germanium isotopic fractionation.

Data Availability Statement: Data are contained within the article and Supplementary Materials.

Acknowledgments: The supercomputer time provided by the CTI-CSIC center is greatly acknowledged. F.C. wants to thank V. Timón for the help during the realization of this work.

Conflicts of Interest: The authors declare no conflicts of interest.

References

1. Atkins, M.; Glasser, F.P. Application of portland cement-based materials to radioactive waste immobilization. *Waste Manag.* **1992**, *12*, 105–131. [CrossRef]
2. Chapman, N.; McCombie, C. Safety and Security Issues in Deep Geological Disposal. In *Principles and Standards for the Disposal of Long-Lived Radioactive Wastes*; Waste Management Series; Elsevier: Amsterdam, The Netherlands, 2003. [CrossRef]
3. Faucon, P.; Adenot, F.; Jacquinot, J.C.; Petit, J.C.; Cabrillac, R.; Jorda, M. Long-term behavior of cement pastes used for nuclear waste disposal: Review of physico-chemical mechanisms of water degradation. *Cem. Concr. Res.* **1998**, *28*, 847–857. [CrossRef]
4. Harfouche, M.; Wieland, E.; Dähn, R.; Fujita, T.; Tits, J.; Kunz, D.; Tsukamoto, M. EXAFS study of U(VI) uptake by calcium silicate hydrates. *J. Colloid Interface Sci.* **2006**, *303*, 195–204. [CrossRef] [PubMed]
5. Ochs, M.; Mallants, D.; Wang, D. *Radionuclide and Metal Sorption on Cement and Concrete*; Springer International Publishing: Berlin, Germany, 2016; Available online: https://link.springer.com/book/10.1007/978-3-319-23651-3 (accessed on 2 January 2024).
6. Mandaliev, P.; Stumpf, T.; Tits, J.; Dähn, R.; Walther, C.; Wieland, E. Uptake of Eu (III) by 11 Ångstrom tobermorite and xonotlite: A TRLFS and EXAFS study. *Geochim. Cosmochim. Acta* **2011**, *75*, 2017–2029. [CrossRef]
7. Gaona, X.; Kulik, D.A.; Macé, N.; Wieland, E. Aqueous–solid solution thermodynamic model of U(VI) uptake in C–S–H phases. *Appl. Geochem.* **2012**, *27*, 81–95. [CrossRef]
8. Pointeau, I.; Landesman, C.; Giffaut, E.; Reiller, P. Reproducibility of the uptake of U(VI) onto degraded cement pastes and calcium silicate hydrate phases. *Radiochim. Acta* **2004**, *92*, 645–650. [CrossRef]
9. Stumpf, T.; Tits, J.; Walther, C.; Wieland, E.; Fanghänel, T. Uptake of trivalent actinides (curium(III)) by hardened cement paste: A time-resolved laser fluorescence spectroscopy study. *J. Colloid Interface Sci.* **2004**, *276*, 118–124. [CrossRef] [PubMed]
10. Tits, J.; Wieland, E. Actinide Sorption by Cementitious Materials. PSI report Nr. 18-02; Paul Scherrer Institut (PSI): Villigen, Switzerland, 2018.
11. Wieland, E.; Macé, N.; Dähn, R.; Kunz, D.; Tits, J. Macro- and micro-scale studies on U(VI) immobilization in hardened cement paste. *J. Radioanal. Nucl. Chem.* **2010**, *286*, 793–800. [CrossRef]
12. Wesselsky, A.; Jensen, O.M. Synthesis of pure Portland cement phases. *Cem. Concr. Res.* **2009**, *39*, 973–980. [CrossRef]
13. Glasser, F.P.; Marchand, J.; Samson, E. Durability of concrete—Degradation phenomena involving detrimental chemical reactions. *Cem. Concr. Res.* **2008**, *38*, 226–246. [CrossRef]
14. Yan, W.; Wei, H.G.; Muchiri, N.D.; Li, F.L.; Zhang, J.R.; Xu, Z.X. Degradation of chemical and mechanical properties of cements with different formulations in CO_2-containing HTHP downhole. *Petrol. Sci.* **2003**, *20*, 1119–1128. [CrossRef]
15. Berner, U.R. Evolution of pore water chemistry during degradation of cement in a radioactive waste repository environment. *Waste Manag.* **1992**, *12*, 201–219. [CrossRef]
16. Thomas, J.J.; Biernacki, J.J.; Bullard, J.W.; Bishnoi, S.; Dolado, J.S.; Scherer, G.W.; Luttge, A. Modeling and simulation of cement hydration kinetics and microstructure development. *Cem. Concr. Res.* **2011**, *41*, 1257–1278. [CrossRef]
17. Scrivener, K.; Ouzia, A.; Juilland, P.; Mohamed, A.K. Advances in understanding cement hydration mechanisms. *Cem. Concr. Res.* **2019**, *124*, 105823. [CrossRef]
18. Zhu, Y.; Mac, Y.; Hu, J.; Zhang, Z.; Huang, J.; Wang, Y.; Wang, H.; Cai, W.; Huang, H.; Yu, Q.; et al. Adsorption of organic core-shell corrosion inhibitors on cement particles and their influence on early age properties of fresh cement paste. *Cem. Concr. Res.* **2020**, *130*, 106000. [CrossRef]
19. Bessaies-Bey, H.; Baumann, R.; Schmitz, M.; Radler, M.; Roussel, N. Organic admixtures and cement particles: Competitive adsorption and its macroscopic rheological consequences. *Cem. Concr. Res.* **2016**, *80*, 1–9. [CrossRef]
20. Bleyen, N.; Van Gompel, V.; Smets, S.; Eyley, S.; Verwimp, W.; Thieleman, W.; Valcke, E. Radiolytic degradation of cellulosic materials in nuclear waste: Effect of oxygen and absorbed dose. *Radiat. Phys. Chem.* **2023**, *212*, 111177. [CrossRef]
21. Nägele, E. The zeta—Potential of cement, Part II. *Effect of pH-Value, Cem. Concr. Res.* **1986**, *15*, 853–863. [CrossRef]

22. Nybo, E.; Maiera, R.S.; Lauchnorb, E.G.; Seymoura, J.D.; Sarah, L.; Codd, S.L. Electrophoretic nuclear magnetic resonance measurement of electroosmotic flow and dispersion in hydrating cement paste. *Cem. Concr. Res.* **2019**, *116*, 11–18. [CrossRef]
23. Hodne, H.; Saasen, A. The effect of the cement zeta potential and slurry conductivity on the consistency of oilwell cement slurries. *Cem. Concr. Res.* **2000**, *30*, 1767–1772. [CrossRef]
24. Holmes, N.; Tyrer, M.; West, R.; Lowe, A.; Kelliher, D. Using PHREEQC to model cement hydration. *Constr. Build. Mater.* **2022**, *319*, 126129. [CrossRef]
25. Skibsted, J.; Hall, C. Characterization of cement minerals, cements and their reaction products at the atomic and nano scale. *Cem. Concr. Res.* **2008**, *38*, 205–225. [CrossRef]
26. Krattiger, N.; Lothenbach, B.; Churakov, S.V. Sorption and electrokinetic properties of ASR product and C-S-H: A comparative modelling study. *Cem. Concr. Res.* **2021**, *146*, 106491. [CrossRef]
27. Macé, N.; Wieland, E.; Dähn, R.; Tits, J.; Scheinost, A.C. EXAFS investigation on U (VI) immobilization in hardened cement paste: Influence of experimental conditions on speciation. *Radiochim. Acta* **2013**, *101*, 379–389. [CrossRef]
28. Baquerizo, L.G.; Matschei, T.; Scrivener, K.L. Impact of water activity on the stability of ettringite. *Cem. Concr. Res.* **2016**, *79*, 31–44. Available online: https://www.sciencedirect.com/science/article/pii/S0008884615001970 (accessed on 2 January 2024). [CrossRef]
29. Renaudin, G.; Segni, R.; Mentel, D.; Nedelec, J.-M.; Leroux, F.; Taviot-Gueho, C. A Raman study of the sulfated cement hydrates: Ettringite and monosulfoaluminate. *J. Adv. Concr. Technol.* **2007**, *5*, 299–312. [CrossRef]
30. Yorkshire, A.S.; Stennett, M.C.; Walkley, B.; O'Sullivan, S.E.; Mottram, L.M.; Bailey, D.J.; Provis, J.L.; Hyatta, N.C.; Corkhil, C.L. Spectroscopic evaluation of UVI–cement mineral interactions: Ettringite and hydrotalcite. *J. Synchrotron Radiat.* **2022**, *29*, 89–102. Available online: https://journals.iucr.org/s/issues/2022/01/00/yw5003/index.html (accessed on 1 January 2022). [CrossRef]
31. Henocq, P. A sorption model for alkalis in cement-based materials—Correlations with solubility and electrokinetic properties. *Phys. Chem. Earth* **2017**, *99*, 184–193. [CrossRef]
32. de Burgh, J.M.; Foster, S.J.; Valipour, H.R. Prediction of water vapour sorption isotherms and microstructure of hardened Portland cement pastes. *Cem. Concrete Res.* **2016**, *81*, 134–150. [CrossRef]
33. Schlegel, M.L.; Pointeau, I.; Coreau, N.; Reiller, P. Mechanism of europium retention by calcium silicate hydrates: An EXAFS study. *Environ. Sci. Technol.* **2004**, *38*, 4423–4431. [CrossRef]
34. Missana, T.; Almendros-Ginestà, O.; Colmenero, F.; Fernández, A.M.; García-Gutiérrez, M. Investigation of the surface charge behaviour of ettringite: Influence of pH, calcium, and sulphate ions. *Heliyon* **2024**, accepted. [CrossRef]
35. Zhang, C.; Liu, L.; Dai, Y.; Zhu, K.; Liu, Z.; Jia, H. Molecular dynamics simulations of ex-change behavior of radionuclides into montmorillonite: Unraveling the dynamic processes and micro-scopic structures. *Appl. Clay Sci.* **2022**, *226*, 106579. [CrossRef]
36. Liu, X.; Cheng, J.; Sliuprik, M.; Lu, X.; Wang, R. Surface acidity of 2:1-type dioctahedral clay minerals from first principles molecular dynamics simulations. *Geochim. Cosmochim. Acta* **2014**, *140*, 410–417. [CrossRef]
37. Gimmi, T.; Churakov, S.V. Water retention and diffusion in unsaturated clays: Connecting atomistic and pore scale simulations. *Appl. Clay Sci.* **2019**, *175*, 169–183. [CrossRef]
38. Kéri, A.; Dähn, R.; Fernandes, M.M.; Scheinost, A.C.; Krack, M.; Churakov, S.V. Iron Adsorption on Clays Inferred from Atomistic Simulations and X-ray Absorption Spectroscopy. *Environ. Sci. Technol.* **2020**, *54*, 11886–11893. [CrossRef]
39. Machesky, M.L.; Predota, M.; Wesolowski, D.J.; Vlcek, L.; Cummings, P.T.; Rosenqvist, J.; Ridley, M.K.; Kubicki, J.D.; Bandura, A.V.; Kumar, N.; et al. Surface Protonation at the Rutile (110) Interface: Explicit Incorporation of Solvation Structure within the Refined MUSIC Model Framework. *Langmuir* **2008**, *24*, 12331–12339. [CrossRef]
40. Orucoglu, E.; Grangeon, S.; Gloter, A.; Robinet, J.C.; Madé, B.; Tournassat, C. Competitive Adsorption Processes at Clay Mineral Surfaces: A Coupled Experimental and Modeling Approach. *ACS Earth Space Chem.* **2022**, *6*, 144–159. [CrossRef]
41. Lin, L.; Huang, J.; Yu, W.; He, C.; Tao, H.; Xu, Y.; Zhu, L.; Wang, P.; Zhang, Z. A periodic DFT study on adsorption of small molecules (CH_4, CO, H_2O, H_2S, NH_3) on the WO_3 (001) surface-supported Au. *Commun. Theor. Phys.* **2020**, *72*, 035501. Available online: https://iopscience.iop.org/article/10.1088/1572-9494/ab690d (accessed on 2 January 2024). [CrossRef]
42. Rutkai, G.; Ható, Z.; Kristof, T. Stability of the kaolinite-guest molecule intercalation system: A molecular simulation study. *Fluid Phase Equiv.* **2016**, *409*, 434–438. [CrossRef]
43. Qiu, S.; Qiu, T.; Yan, H.; Long, Q.; Wu, H.; Li, X.; Zhu, D. Investigation of protonation and deprotonation processes of kaolinite and its effect on the adsorption stability of rare earth elements. *Colloids Surf. A* **2022**, *642*, 128596. [CrossRef]
44. Kalinichev, A.G.; Kirkpatrick, R.J. Molecular dynamics modeling of chloride binding to the surfaces of calcium hydroxide, hydrated calcium aluminate, and calcium silicate phases. *Chem. Mater.* **2022**, *14*, 3539–3549. [CrossRef]
45. Kalinichev, A.G.; Wang, J.W.; Kirkpatrick, R.J. Molecular dynamics modeling of the structure, dynamics and energetics of mineral-water interfaces: Application to cement materials. *Cem. Concr. Res.* **2007**, *37*, 337–347. [CrossRef]
46. Kirkpatrick, R.J.; Kalinichev, A.G.; Hou, X.; Struble, L. Experimental and molecular dynamics modeling studies of interlayer swelling: Water incorporation in kanemite and ASR gel. *Mater. Struct.* **2005**, *38*, 449–458. [CrossRef]
47. Androniuk, I.; Landesman, C.; Henocq, P.; Kalinichev, A.G. Adsorption of gluconate and uranyl on C-S-H phases: Combination of wet chemistry experiments and molecular dynamics simulations for the binary systems. *Phys. Chem. Earth* **2017**, *99*, 194–203. [CrossRef]
48. Zhao, H.; Yang, Y.; Shu, X.; Wang, T.; Ran, Q. Comparison of Adsorption Conformation of Comb-Shaped Polycarboxylate on Tricalcium Aluminate (100) and Ettringite (100) Surfaces: A Molecular Dynamics Study. *Adv. Theory Simul.* **2021**, *4*, 2100079. [CrossRef]

49. Goyal, A.; Palaia, I.; Ioannidou, K.; Ulm, F.J.; van Damme, H.; Pellenq, R.J.M.; Trizac, E.; Del Gado, E. The physics of cement cohesion. *Sci. Adv.* **2021**, *7*, eabg5882. Available online: https://www.science.org/doi/10.1126/sciadv.abg5882 (accessed on 2 January 2024). [CrossRef] [PubMed]
50. Tararushkin, E.V.; Pisarev, V.V.; Kalinichev, A.G. Atomistic simulations of ettringite and its aqueous interfaces: Structure and properties revisited with the modified ClayFF force field. *Cem. Concr. Res.* **2022**, *156*, 106759. [CrossRef]
51. Bahraq, A.A.; Al-Osta, M.A.; Al-Amoudi, O.S.B.; Obot, I.B.; Maslehuddin, M.; Ahmed, H.R.; Saleh, T.A. Molecular Simulation of Cement-Based Materials and Their Properties. *Engineering* **2022**, *15*, 165–178. [CrossRef]
52. Mutisya, S.M.; de Almeida, J.M.; Miranda, C.R. Molecular simulations of cement based materials: A comparison between first principles and classical force field calculations. *Comput. Mater. Sci.* **2017**, *138*, 392–402. [CrossRef]
53. Churakov, S.V.; Labbez, C.; Pegado, L.; Sulpizi, M. Intrinsic acidity of surface sites in calcium silicate hydrates and its implication to their electrokinetic properties. *J. Phys. Chem. C* **2014**, *118*, 11752–11762. [CrossRef]
54. Kremleva, A.; Krüger, S.; Rösch, N. Uranyl(VI) sorption in calcium silicate hydrate phases. A quantum chemical study of tobermorite models. *Appl. Geochem.* **2020**, *113*, 104463. [CrossRef]
55. Guo, B.; Xiong, Y.; Chen, W.; Saslow, S.A.; Kozaid, N.; Ohnukid, T.; Dabo, I.; Sasaki, K. Spectroscopic and first-principles investigations of iodine species incorporation into ettringite: Implications for iodine migration in cement waste forms. *J. Hazard. Mater.* **2020**, *389*, 121880. [CrossRef]
56. Silva Andrade Neto, J.; De la Torre, A.G.; Kirchheim, A.P. Effects of sulfates on the hydration of Portland cement—A review. *Constr. Build. Mater.* **2021**, *279*, 122428. [CrossRef]
57. Moore, A.; Taylor, H.F. Crystal structure of ettringite. *Nature* **1988**, *218*, 1048–1049. [CrossRef]
58. Hartman, M.R.; Berliner, R. Investigation of the structure of ettringite by time-of-flight neutron powder diffraction techniques. *Cem. Concr. Res.* **2006**, *6*, 364–370. [CrossRef]
59. Goetz-Neunhoeffer, F.; Neubauer, J. Refined ettringite ($Ca_6Al_2(SO_4)_3(OH)_{12}\cdot 26H_2O$) structure for quantitative X-ray diffraction analysis. *Powder Diffr.* **2006**, *21*, 4–11. [CrossRef]
60. Gatta, G.D.; Hålenius, U.; Bosi, F.; Cañadillas-Delgado, L.; Fernandez-Diaz, M.T. Minerals in cement chemistry: A single-crystal neutron diffraction study of ettringite, $Ca_6Al_2(OH)_{12}(SO_4)_3\cdot 27H_2O$. *Amer. Mineral.* **2019**, *104*, 73–78. Available online: https://pubs.geoscienceworld.org/msa/ammin/article-abstract/104/1/73/567952 (accessed on 2 January 2024). [CrossRef]
61. Zhang, M.; Reardon, A.J. Removal of B, Cr, Mo, and Se from Wastewater by Incorporation into Hydrocalumite and Ettringite. *Environ. Sci. Technol.* **2003**, *37*, 2947–2952. [CrossRef]
62. Myneni, S.C.B.; Traina, S.J.; Logan, T.J.; Waychunas, G.A. Oxyanion Behavior in Alkaline Environments: Sorption and Desorption of Arsenate in Ettringite. *Environ. Sci. Technol.* **1997**, *31*, 1761–1768. [CrossRef]
63. Baur, S.; Johnson, C.A. Sorption of Selenite and Selenate to Cement Minerals. *Environ. Sci. Technol.* **2003**, *37*, 3442–3447. [CrossRef]
64. Evans, N.M.D. Binding mechanisms of radionuclides to cement. *Cem. Concr. Res.* **2008**, *38*, 543–553. [CrossRef]
65. Chen, Q.Y.; Tyrer, M.; Hills, C.D.; Yang, X.M.; Carey, P. Immobilisation of heavy metal in cement-based solidification/stabilisation: A review. *Waste Manag.* **2009**, *29*, 390–403. [CrossRef] [PubMed]
66. Zhao, Y.; Sun, Y.; Guo, Z.; Qiu, J.; Sun, X. First-principles investigations of arsenate doping into the ettringite lattice. *J. Clean. Prod.* **2023**, *419*, 138266. [CrossRef]
67. Dezerald, L.; Kohanoff, J.J.; Correa, A.A.; Caro, A.; Pellenq, R.J.M.; Ulm, F.J.; Saúl, A. Cement As a Waste Form for Nuclear Fission Products: The Case of ^{90}Sr and Its Daughters. *Environ. Sci. Technol.* **2015**, *49*, 13676–13683. [CrossRef] [PubMed]
68. Polettini, A.; Pomi, R.; Sirini, P. Fractional factorial design to investigate the influence of heavy metals and anions on acid neutralization behavior of cement-based products. *Environ. Sci. Technol.* **2002**, *36*, 1584–1591. [CrossRef] [PubMed]
69. Bonen, D.; Sarkar, S.L. The effects of simulated environmental attack on immobilization of heavy metals doped in cement-based materials. *J. Hazard. Mater.* **1995**, *40*, 321–335. [CrossRef]
70. Barger, G.S.; Bayles, J.; Blair, B.; Brown, D.; Chen, H.; Conway, T.; Hawkins, P.; Helinski, R.A.; Innis, F.A.; Luther, M.D.; et al. Ettringite Formation and the Performance of Concrete. Portland Cement Association, 2001. Available online: https://www.semanticscholar.org/paper/Ettringite-Formation-and-the-Performance-of/c230c26eaa591ed43198868c39a706fafe772122 (accessed on 2 January 2024).
71. Prince, W.; Espagne, M.; Aïtkin, P.C. Ettringite formation: A crucial step in cement superplasticizer compatibility. *Cem. Concr. Res.* **2003**, *33*, 635–641. [CrossRef]
72. Speziale, S.; Jiang, F.; Mao, Z.; Monteiro, P.J.M.; Wenk, H.R.; Duffy, T.S.; Schilling, F.R. Single-crystal elastic constants of natural ettringite. *Cem. Concr. Res.* **2008**, *38*, 885–889. [CrossRef]
73. Clark, S.M.; Colas, B.; Kunz, M.; Speziale, S.; Monteiro, P.J.M. Effect of pressure on the crystal structure of ettringite. *Cem. Concr. Res.* **2008**, *38*, 19–26. [CrossRef]
74. Sun, W.; Wang, D.; Wang, L. Molecular Dynamic Simulation of Failure of Ettringite, Molecular Dynamic Simulation of Failure of Ettringite. *J. Phys. Conf. Ser.* **2013**, *419*, 012011. [CrossRef]
75. Stroh, J.; Ali, N.Z.; Maierhofer, C.; Emmerling, F. Ettringite via Mechanochemistry: A Green and Rapid Approach for Industrial Application. *ACS Omega* **2019**, *4*, 7734–7737. [CrossRef] [PubMed]
76. Scholtzová, E.; Kucková, L.; Kozisek, J.; Tunega, D. Structural and spectroscopic characterization of ettringite mineral combined DFT and experimental study. *J. Mol. Struct.* **2015**, *1100*, 215–224. [CrossRef]

77. Scholtzová, E.; Tunega, D.; Speziale, S. Mechanical properties of ettringite and thaumasite—DFT and experimental study. *Cem. Concr. Res.* **2015**, *77*, 9–15. [CrossRef]
78. Damidot, D.; Barnett, S.J.; Barnett, F.; Glasser, F.; Macphee, D.; Macphe, D. Investigation of the $CaO–Al_2O_3–SiO_2–CaSO_4–CaCO_3–H_2O$ system at 25 °C by thermodynamic calculation. *Adv. Cem. Res.* **2004**, *16*, 69–76. [CrossRef]
79. Perkins, R.B.; Palmer, C.D. Solubility of ettringite $Ca_6Al_2(OH)_{12}(SO_4)_3{\cdot}26H_2O$ at 5–75 °C. *Geochim. Cosmochim. Acta* **1999**, *63*, 1969–1980. [CrossRef]
80. Álvarez-Ayuso, E.; Nugteren, H.W. Synthesis of ettringite: A way to deal with the acid wastewaters of aluminium anodising industry. *Water Res.* **2005**, *39*, 65–72. [CrossRef] [PubMed]
81. Odler, I.; Abdul-Maula, S. Possibilities of quantitative determination of the AFt-(ettringite) and AFm-(monosulphate) phases in hydrated cement pastes. *Cem. Concr. Res.* **1984**, *14*, 133–141. [CrossRef]
82. Warren, C.J.; Reardon, E.J. The solubility of ettringite at 25 °C. *Cem. Concr. Res.* **1994**, *24*, 1515–1524. [CrossRef]
83. ICDD. The International Centre for Diffraction Data. 2023. Available online: https://www.icdd.com (accessed on 2 January 2024).
84. Omnic. OMNIC Series Software for Spectroscopy, Elemental & Isotope Analysis. 2023. Available online: https://www.thermofisher.com/order/catalog/product/INQSOF018 (accessed on 2 January 2024).
85. Clark, S.J.; Segall, M.D.; Pickard, C.J.; Hasnip, P.J.; Probert, M.I.J.; Refson, K.; Payne, M.C. First Principles Methods Using CASTEP. *Z. Kristallogr.* **2005**, *220*, 567–570. [CrossRef]
86. MaterialsStudio. 2024. Available online: https://3dsbiovia.com/products/collaborative-science/biovia-materials-studio/ (accessed on 2 January 2024).
87. Payne, M.C.; Teter, M.P.; Ailan, D.C.; Arias, A.; Joannopoulos, J.D. Iterative minimization techniques for ab initio total-energy calculations: Molecular dynamics and conjugate gradients. *Rev. Mod. Phys.* **1992**, *64*, 1045–1097. [CrossRef]
88. Perdew, J.P.; Burke, K.; Ernzerhof, M. Generalized Gradient Approximation Made Simple. *Phys. Rev. Lett.* **1996**, *77*, 3865–3868. [CrossRef] [PubMed]
89. Grimme, S. Semiempirical GGA-type Density Functional Constructed with a Long-Range Dispersion Correction. *J. Comput. Chem.* **2006**, *27*, 1787–1799. [CrossRef] [PubMed]
90. Troullier, N.; Martins, J.L. Efficient Pseudopotentials for Plane-Wave Calculations. *Phys. Rev. B* **1991**, *43*, 1993–2006. [CrossRef]
91. Monkhorst, H.J.; Pack, J.D. Special Points for Brillouin-zone Integration. *Phys. Rev. B* **1976**, *13*, 5188–5192. [CrossRef]
92. Pfrommer, B.G.; Cote, M.; Louie, S.G.; Cohen, M.L. Relaxation of Crystals with the Quasi-Newton Method. *J. Comput. Phys.* **1997**, *131*, 233–240. [CrossRef]
93. REFLEX. 2024. Available online: https://www.3ds.com/fileadmin/PRODUCTS-SERVICES/BIOVIA/PDF/BIOVIA-material-studio-reflex.pdf (accessed on 2 January 2024).
94. Downs, R.T.; Bartelmehs, K.L.; Gibbs, G.V.; Boisen, M.B. Interactive software for calculating and displaying X-ray or neutron powder diffractometer patterns of crystalline materials. *Am. Mineral.* **1993**, *78*, 1104–1107.
95. Baroni, S.; de Gironcoli, S.; Dal Corso, A. Phonons and Related Crystal Properties from Density-Functional Perturbation Theory. *Rev. Mod. Phys.* **2001**, *73*, 515–562. [CrossRef]
96. Refson, K.; Tulip, P.R.; Clark, S.J. Variational Density-Functional Perturbation Theory for Dielectrics and Lattice Dynamics. *Phys. Rev. B* **2006**, *73*, 155114. [CrossRef]
97. Adsorption Locator. A Module of BIOVIA Materials Studio Package of Programs (Dassault Systemes). 2024. Available online: https://www.gga.asia/upload/pdf/484/adsorption-locator_20170927140829%20(1).pdf (accessed on 2 January 2024).
98. Akkermans, R.L.C.; Spenley, N.A.; Robertson, S.H. COMPASS III: Automated fitting workflows and extension to ionic liquids. *Mol. Simul.* **2021**, *47*, 540–551. [CrossRef]
99. Sun, H. COMPASS: An ab Initio Force-Field Optimized for Condensed-Phase Applications—Overview with Details on Alkane and Benzene Compounds. *J. Phys. Chem. B* **1998**, *102*, 7338–7364. [CrossRef]
100. Frost, R.L.; López, A.; Xi, Y.; Scholz, R.; Magela da Costac, G.; Fernandes Lima, R.; Granja, A. The spectroscopic characterization of the sulphate mineral ettringite from Kuruman manganese deposits, South Africa. *Vib. Spectrosc.* **2013**, *68*, 266–271. [CrossRef]
101. Myneni, S.C.B.; Traina, S.J.; Glenn, A.; Waychunas, G.A.; Logan, T.J. Experimental and theoretical vibrational spectroscopic evaluation of arsenate coordination in aqueous solutions, solids, and at mineral-water interfaces. *Geochim. Cosmochim. Acta* **1991**, *62*, 3285–3300. [CrossRef]
102. Hartkamp, R.; Biance, A.L.; Fu, L.; Dufrêche, J.F.; Bonhomme, O.; Joly, L. Measuring surface charge: Why experimental characterization and molecular modeling should be coupled. *Curr. Opin. Colloid Interface Sci.* **2018**, *37*, 101–114. [CrossRef]
103. Shi, C.S.; Zhang, G.; He, T.; Li, Y. Effects of superplasticizers on the stability and morphology of ettringite. *Constr. Build. Mater.* **2016**, *112*, 261–266. [CrossRef]
104. Manzano, H. Atomistic simulations applications in cement and related building materials. *Cem. Concr. Res.* **2022**, *156*, 106998. [CrossRef]
105. Manzano, H.; Ayuela, A.; Telesca, A.; Monteiro, P.J.M.; Dolado, J.S. Ettringite strengthening at high pressures induced by the densification of the hydrogen bond network. *J. Phys. Chem.* **2012**, *116*, 16138–16143. [CrossRef]
106. Skoblinskaya, N.N.; Krasilnikov, K.G. Changes in crystal structure of ettringite on dehydration. *Cem. Concr. Res.* **1975**, *5*, 381–394. [CrossRef]
107. Renaudin, G.; Filinchuk, Y.; Neubauer, J.; Goetz-Neunhoeffer, F. A comparative structural study of wet and dried ettringite. *Cem. Concr. Res.* **2010**, *40*, 370–375. [CrossRef]

108. Shimada, Y.; Young, J.F. Structural changes during thermal dehydration of ettringite. *Adv. Cem. Res.* **2001**, *13*, 77–81. [CrossRef]
109. Hall, C.; Barnes, P.; Billimore, A.D.; Jupe, A.C.; Turrillas, X. Thermal decomposition of ettringite $Ca_6[Al(OH)_6]_2(SO_4)_3 \cdot 26H_2O$. *J. Chem. Soc. Faraday Trans.* **1996**, *92*, 2125–2129. [CrossRef]
110. Kißling, P.A.; Lübkemann, F.; von Bronk, T.; Cotardo, D.; Lei, L.; Feldhoff, A.; Lohaus, L.; Haist, M.; Bigall, N.C. Influence of Low-Pressure Treatment on the Morphological and Compositional Stability of Microscopic Ettringite. *Materials.* **2021**, *14*, 2720. [CrossRef] [PubMed]
111. Wang, Q.; Manzano, H.; López-Arbeloa, I.; Shen, I. Water Adsorption on the β-Dicalcium Silicate Surface from DFT Simulations. *Minerals* **2018**, *8*, 386. [CrossRef]